Generation of a single hot spot by use of a deformable mirror and study of its propagation in an underdense plasma

Benoit Wattellier,* Julien Fuchs,† Ji-Ping Zou, Jean-Christophe Chanteloup, Heidi Bandulet, Pierre Michel,‡and Christine Labaune

Laboratoire pour l'Utilisation des Lasers Intenses, Unité Mixte de Recherche 7605 du Centre National de la Recherche Scientifique—Ecole Polytechnique Commissariat à l'Energie Atomique, Université Paris VI, Ecole Polytechnique, 91128 Palaiseau Cedex, France

Sylvie Depierreux

Commissariat à l'Energie Atomique–Direction Ile-de-France, B.P. 12, 91680 Bruyères Le Châtel, France

Alexis Kudryashov and Alexander Aleksandrov

Adaptive Optics for Industrial and Medical Applications Group, Russian Academy of Sciences, Moscow 117333, Russia

Received December 6, 2002; revised manuscript received March 20, 2003

Adaptive optics systems offer the prospect of significantly increasing the capabilities of high-power laser focusability, which is currently limited by thermal distortions. Using novel wave-front measurement techniques that improve the stability of such systems and a downstream large-aperture deformable mirror that does not bear the usual limitations associated with precompensation, we have improved the focusability of a high-power (6×100-J, 1-ns) Nd:glass laser facility by a factor of 6. Measuring the wave front and the on-target focal spot at full power, we obtained after correction focal spots with a best Strehl ratio of 0.6. The pulse peak intensity could thus be increased to $\sim2\times10^{16}$ W/cm^2, a level beyond reach of the usual focal spot shaping techniques. We then used the near-diffraction-limited focal spots produced by this system to measure the laser–plasma coupling for a single, controlled filament of light and to underline the importance of the coupling among the numerous speckles within conventional multispeckled beams.

OCIS codes: 010.1080, 140.3580, 350.4990, 140.6810, 190.3100.

1. INTRODUCTION

Flash-lamp-pumped high-energy solid-state lasers are limited in terms of focusability by thermal effects. Because most of the broadband flash-lamp energy cannot be transferred to the laser pulses, it is dissipated as heat in the amplifiers. The consequent temperature rise deforms the amplifying materials,[1] which results in disturbance of the laser pulse's wave front. Such low-order aberrations are usually not eliminated by spatial filtering. To maintain relatively good beam quality one must thus wait for the amplifiers to thermalize before firing the next shot. For instance, most 100-J laser systems have a repetition rate of no more than one laser shot every 20 min.

However, even if one allows time for the amplifiers to cool between successive shots, the pump-induced thermal shock is still enough to significantly deform the wave front of the amplified laser pulse. Under the best conditions, it still spreads a large fraction of the energy in a halo about the central focal spot.[2] In our 6×100-J laser system at the Laboratoire pour l'Utilisation des Lasers Intenses (LULI) the beam is so aberrated that the expected Airy pattern is split into several hot spots [see Fig. 1(a) for a focal spot of a typical 80-J shot], for all of which the peak intensities are of the same order of magnitude. Moreover, because of air disturbance and room-temperature and flash-lamp fluctuations, the overall pattern can also change from day to day.

For the field of application that is of interest to us, i.e., laser–plasma interaction physics[3] (LPI) for inertial confinement fusion[4,5] (ICF), using such irregularly speckled focal patterns is of low interest. For ICF, large and smooth focal patterns with long-scale intensity gradients are required[4] for prevention of strong growth of hydrodynamic or parametric instabilities and to ensure homogeneous illumination of the target.

Over the past two decades much effort has been devoted to increasing the focal spot homogeneity of high-power lasers and to obtaining generic (i.e., comparable from one facility to another) interaction conditions. Random phase plates (RPPs) have been used to decrease the transverse coherence of the laser beam.[6] The resultant focal spot[7] [see Fig. 1(b)] is large, more than ten times larger than the diffraction limit, with small-scale structures (speckles of various intensities) within a long-scale smooth envelope. More recently, other techniques have been put forward to further decrease the spatial[8–11] and

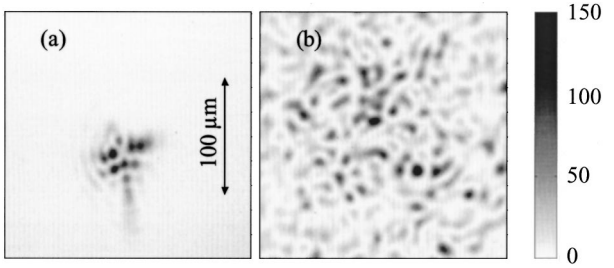

Fig. 1. Far-field patterns of a high-energy shot (80 J) recorded with an $f = 500$ mm doublet. The incident beam's diameter is 85 mm. In (b) a random phase plate (2-mm elements) has been added before the focusing doublet (low-energy shot).

temporal[10–13] coherence of the laser beam and to improve the focal pattern's homogeneity.

Such smoothed beams, currently planned to be used in the future megajoule-scale ICF facilities, however, still have speckles with local intensities a few times the average intensity. Performing laser–plasma interaction studies with a beam composed of only a single hot spot (SHS), whose size matches that of one of the speckles within the RPP-produced focal distribution, is therefore of great interest for the study of fundamental interaction physics. Indeed, the results obtained in this way represent the sole action of a deterministic single hot spot within the plasma and not an average response to an interdependent ensemble of speckles that have various intensities. Thus it allows the theoretical models to be validated and the simulation codes to be assessed on a level of reduced complexity. Also, reducing the needed size of the simulation boxes[14] permits realistic situations that correspond to the experiments to be simulated in a reasonable time. Another interesting property of the SHS configuration is that it permits the study of local effects such as filament instabilities[15–18] and local transport properties[19–21] that cannot be observed with large, multispeckled beams. Finally, the SHS configuration is also of interest because gathering all the energy into one unique focal spot results in a peak intensity that is, for the same input energy, at least 2 orders of magnitude higher than with the usual laser smoothing techniques. In this way, new interaction regimes can be reached by use of medium-scale facilities such as ours at the LULI.

One can produce a diffraction-limited SHS by reducing the beam size to get a small enough aperture that the inside of the phase is approximately flat.[22,23] This, however, limits the available energy because only a fraction of the high-energy beam is used. Alternatively, wave-front correction techniques, first developed for astronomy,[24] can produce the same result while they keep the beam's full energy. Wave-front correction is usually achieved through an adaptive optics loop that uses a sensor and a corrector to lock the wave front toward a reference (usually flat). Several groups of researchers have applied these techniques to high-power lasers, yet their work is still incomplete. Druon *et al.*[25] demonstrated wave-front correction on a short-pulse laser but did not actually measure and characterize the resultant focal spot. Pennington *et al.*[26] used an adaptive optics loop on the Lawrence Livermore National Laboratory NOVA petawatt laser chain. They did not characterize the on-target full power focal spot because their far-field measurement relied on an equivalent plane imaging. Moreover, the correction capacity of their adaptive optic loop (based on a dielectric-coated electrostrictive deformable mirror) was limited by their deformable mirror's aperture: Because it was relatively small, it had to be put upstream in the NOVA amplifying chain. In such a position, the mirror had to precompensate for the aberrations induced along propagation. The diameter of the spatial filter pinholes then had to be increased, resulting in a high-spatial-frequency noise that was propagated up to the target and created a pedestal in the far-field pattern. Relying on a different kind of corrector, i.e., a liquid-crystal valve, Chanteloup *et al.*[27] achieved good wave-front correction; however, the use of such a valve imposes a strong limitation on the usable beam energy because of the valve's low damage threshold.

In this paper we fully characterize, for the first time to our knowledge, the performance of an adaptive optical system coupled to a high-power (6×100-J, 1-ns) Nd:glass laser by measuring at full power both the on-target focal spot and the corrected wave front. We also show that using an interferometer, i.e., an achromatic three-wave lateral shearing interferometer[28,29] (ATWLSI), as the wave-front sensor significantly improves the stability of the closed loop system compared to that of the Shack–Hartmann (SH) sensors that are usually used.[26] Moreover, our system uses a dielectric-coated bimorphic large-aperture deformable mirror[30,31] placed just before the focusing optics, thus avoiding the limitations associated with a scheme for precompensation of wave-front distortions.[26] We present a comprehensive description of our system through its performance as well as its limitations, showing that the focusability of the laser at full power is improved by a factor of 6, with a best Strehl ratio of 0.6.

In Subsection 2.A we review the elements and techniques that allow us to achieve the correction of one arm of the 6×100-J LULI facility, namely, the adaptive optics loop, the deformable mirror, and the wave-front sensor (i.e., a SH sensor and an ATWLSI). We then describe in Subsection 2.B the 6×100-J nanosecond laser facility at the LULI and in Subsection 2.C present wave-front measurements made with the ATWLSI. Subsection 2.D is devoted to the correction of 80-J laser shots and to discussion of the performance and limitations of our system. Finally, we present in Section 3 some comparative results of the high-intensity propagation of either a single hot spot or an RPP-smoothed, multispeckled beam through an underdense plasma. These results allow us to identify the main nonlinear effects at play in SHS propagation and also to underline the importance of the coupling among the numerous speckles within conventional multispeckled beams, an effect that has been neglected in numerous models of the laser–plasma interaction.

2. WAVE-FRONT CORRECTION AT HIGH ENERGY

A. System Design

A deformable mirror (DM) is a bimorphic mirror with piezoelectric actuators that locally deform a 3-mm-thick glass substrate. The deformations can be as much as ± 3

μm. A piezoelectric piece covers the whole surface (diameter, 98 mm) and corrects general defocus. Thirty other actuators are distributed among three rings with diameters of 42, 73, and 98 mm. We chose the geometry and the number of electrodes on the DM[31] by assessing the aberrations of a typical full-power shot and then calculating how many modes are theoretically needed to flatten the wave front and thereby produce a focal spot with a Strehl ratio[32] of >0.9. The hysteresis of the piezoelectric transducer was estimated to be less than 10% and did not disturb the convergence loops. A reflecting dielectric layer was deposited onto the mirror substrate to prevent any laser-induced damage. Indeed, for a pulse energy of 80 J the laser fluence on the DM was 1.4 J cm^{-2}. With such coating we did not observe any damage on the mirror surface, even after several tens of 80-J shots. We implemented the DM as the last mirror before focalization, so no further aberrations, after correction, could be added by the propagation.

We developed LabView-based software to produce a closed loop between the wave-front sensor and the DM to converge toward a flat wave front for the laser beam.[33] We used a classic response matrix algorithm, which assumes that the mirror response is linear: The effect of two actuators is the sum of the effect of each of them. Linear algebra methods could then be used for calculating the voltages to apply to correct given wave-front aberrations. By addressing one actuator after the other, we obtained a response matrix M_{mn} that links the applied voltage to the measured phase for the ATWLSI or phase gradients for the SH sensor:

$$R_m = M_{mn} V_n , \tag{1}$$

where R_m is the vector composed of the flattened phase maps (we converted the two-dimensional phase maps into a one-dimensional vector by averaging zones of $k*k$ pixels and appending them) retrieved from the phase measurement and V_n is the vector of the voltages applied to the bimorphic actuators. By pseudo-inverting the M_{mn} matrix we could determine the voltages that compensate for wave-front distortions that occur during a shot. The inversion was made by the singular value decomposition (SVD) method that defines a basis of modes onto which we can project the measured phase. Any matrix can be decomposed as a product of three matrices:

$$M_{mn} = P_{mn} S_{nn} {}^t Q_{nn} , \tag{2}$$

where P_{mn} and Q_{nn} are matrices with orthogonal columns, which means that inverting them is transposing them, and S_{nn} is a diagonal matrix that contains so-called singular values. Pseudo-inverting the M_{mn} matrix is then straightforward:

$$M_{nm}{}^{-1} = Q_{nn} (1/s)_{nn} {}^t P_{nm} . \tag{3}$$

The SVD method can be interpreted in this way: P_{mn} contains n mirror modes that correspond to n singular values S_{nn}. The inversion process projects the measured phase onto these modes, assigns to each of them a $(1/s)_n$ weight, and then sums the corresponding Q_{nn} voltages. Looking closer at the singular-value spectrum, we can see that high $(1/s)_n$ weights are associated with highly complex mirror modes, which are extremely sensitive to the noise level. These modes are then amplified by the loop and can make it diverge. The SVD decomposition allows us to filter out these high-leverage modes to stabilize the convergence of the loop.

If the mirror were perfectly linear, we would not need any convergence loop at all. Unfortunately, some nonlinearity such as hysteresis usually occurs when one is working with a deformable mirror. Consequently, to achieve convergence, we do not at once apply the correction voltages deduced from the SVD method but rather apply a gain factor, usually 0.8, to the correction voltages and add the correction voltages to the voltages already applied on the mirror. Using higher gain can make the loop diverge, whereas using a smaller gain slows down the convergence.

We emphasize that our loop is based on the integrated phase map, whereas usual adaptive optic loops, based on the SH sensor, use phase gradients as an input for the response matrix process. This is one of the bases for the improved stability of the system that uses the ATWLSI as the wave-front sensor.

Compared with SH sensors, which are normally used in adaptive optic loops,[26] a loop that uses the ATWLSI proves to be much less sensitive to misalignment: We calculated the response matrix once for a 15-day experiment campaign, whereas when we used a SH sensor we had to measure the response matrix at least every day. Moreover, as the transverse resolution of the ATWLSI is very high (128×128 measurement points), we could downsample the measured phase map to four times the number of actuators on the mirror, that is, 120 measurement points. As a result, the loop became insensitive to misalignment. An additional interesting property of a loop that integrates an ASWLSI is that it can be readily integrated in a short-pulse laser because the ATWLSI is inherently achromatic.

We tested the convergence loop and the mirror with a perfectly collimated cw laser beam from a commercial collimator, using a Nd:YAG laser. This plane wave was used as a reference for the ATWLSI. We replaced one of the mirrors in the optical setup with a deformable mirror. At rest, that is, when no voltage is applied, the surface of the mirror was not flat, which resulted in a poor far-field pattern, as shown in Fig. 2(a). The correction loop converged in less than four iterations and was highly stable. The residual phase after correction was 0.15 λ peak to valley (PtV) and $\lambda/50$ rms ($\lambda = 1064$ nm) when the fluctuation level was $\lambda/300$ rms. Such a correction was limited by the resolution of the mirror. Accordingly, the far-field pattern was much improved, as shown in Fig. 2(b), with a Strehl ratio of 0.85.

We also demonstrated that, to get the best performance from the mirror, we had to use a laser beam aperture limited to 80% of the mirror aperture. This corresponds to half the diameter of the third ring of electrodes, which could thus be still used to perform correction. For larger

apertures the aberrations on the edges could not be compensated for because the constraints on the outer part of the mirror yielded a reduced capacity for local deformations in this area. For smaller apertures the effect of the third ring was not accurately measured with the wave-front sensor, so noise on the corresponding electrode response increased, thus decreasing the ability of the loop to converge. In both cases we observed a deteriorated Strehl ratio for the measured focal spot at the end of the convergence.

B. Implementation of the Loop on the LULI 6 × 100-J Solid-State Laser

The LULI 6 × 100-J laser is an in-line rod-amplifier laser chain. The amplifier material is phosphate glass doped with neodymium (Nd). A Nd:YLF oscillator delivers at a wavelength of $\lambda = 1053$ nm a train of temporally Gaussian pulses of 600-ps FWHM duration. One of these pulses, selected by a Pockels cell, is amplified to ~50 J and split into six arms. Each beam is finally amplified to a maximum of 100 J with a beam diameter of 85 mm, except for the interaction beam, to which a wave-front correction is applied and whose diameter is reduced to 65 mm (it is apodized further than the other beams). The nonlinear B integral[34] accumulated through amplification is 3.0 for full-power shots. Inasmuch as the laser beams propagate over 30 m from the laser room to the experimental hall, this procedure produces strong intensity modulations in the near field, as can be seen from Fig. 3(a).

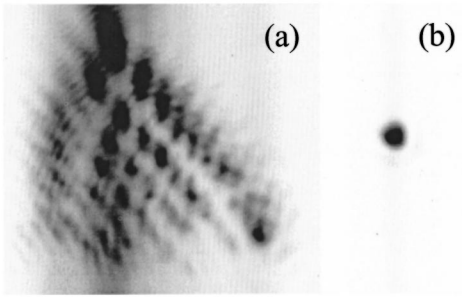

Fig. 2. Far-field patterns in the output of the deformable mirror recorded with a long-focus ($f = 2200$ mm) diffraction-limited lens and a cw laser. (a) The deformable mirror is relaxed. (b) At the end of the closed loop the Strehl ratio reaches 0.85. (Vertical bands visible in both images are due to readout noise onto the CCD.) The two images, recorded at different attenuations, are on the same scale. The beam aperture is limited to 80 mm to match 80% of the deformable mirror's aperture (98 mm).

For the laser–plasma interaction experiments we use four beams to create, heat, and interact with the plasma (see below). Wave-front correction is applied to only one beam, the interaction beam. It is focused on the plasma by an $f_1 = 500$ mm doublet (see Fig. 4). To monitor the far-field pattern of the interaction beam we collect the transmitted beam after the focal point through a 9× telescope (two doublets: $f_2 = 250$ mm and $f_3 = 2200$ mm) combined with a 4× microscope objective. The images are recorded with a 12-bit CCD camera. As the interaction beam diameter is ~65 mm, we expect a diffraction-limited FWHM diameter of ~9 μm.

To produce the closed loop we chose not to address the third (outer) ring of electrodes on the DM. Indeed, for such high-power lasers, because of saturation in the amplifiers the high-energy shots have a super-Gaussian intensity profile, whereas the low-energy shots (those used to determine the response matrix) have a Gaussian shape. Consequently the low-energy shots do not cover the whole surface of the mirror, and the response functions for the third and outer ring of electrodes are much less clearly determined than those for the electrodes within the first two rings. This result, added to the fact that the outer electrodes are the ones associated with the high-frequency modes, induces errors when we want to use them to derive the necessary correction for high-power shots. To discard the third ring of electrodes should not significantly hamper our ability to correct the wave front because with only 15 working electrodes (instead of 30) we could still theoretically[31] reach a Strehl ratio of 0.85. Discarding the ring, however, greatly improved the convergence ability of the loop and its stability.

C. Wave-Front Measurement

We measured the wave fronts of full-power laser shots (70 J) at two locations at the LULI, in the laser hall and in the interaction room, after 30 m of propagation in the air. In the laser hall, the wave-front average PtV was 0.8 λ. At full power, the aberrations are mainly defocus and

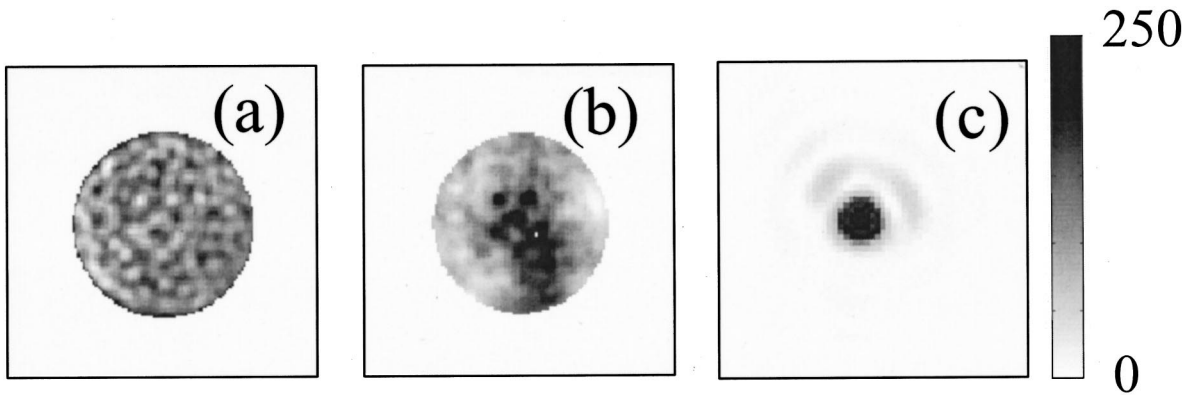

Fig. 3. (a) Intensity and (b) phase maps (the phase PtV is 0.48 λ) for the final state of the convergence [see Fig. 6(d) below] as extracted from the interferogram given by the ATWLSI. These maps are used in calculating (c) the simulated far-field pattern, whose Strehl ratio is 0.7. The gray scale applies only for (c).

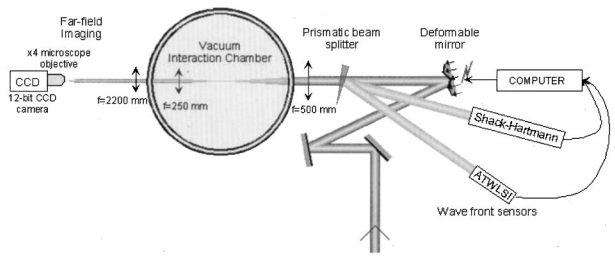

Fig. 4. Setup for wave-front correction. The experiment uses four beams. For clarity, only the interaction beam, to which wave-front correction is applied, is shown. This beam's diameter is 65 mm. It is focused by an $f_1 = 500$ mm doublet. The far field inside the vacuum interaction chamber is imaged by a 9× telescope (two doublets $f_2 = 250$ mm and $f_3 = 2200$ mm) combined with a 4× microscope objective. The images are recorded with a 12-bit CCD camera.

astigmatism.[31] Once the laser chain was thermalized (shots were made in regular sequence), the wave front phase in the laser hall was stable, with shot-to-shot fluctuations of ~0.15λ PtV; i.e., there were no noticeable cumulative heat effects,[1,35] as we show in Fig. 5. In the figure we display two-dimensional maps of the phase difference between a shot in a series and the first shot in the same series. Such differential phase maps are shown for the fourth shot [Fig. 5(a)] and the tenth shot [Fig. 5(b)] of a series of 80-J shots performed at the usual repetition rate of the laser, i.e., a shot every 20 min. To get similar stability of the wave front in the interaction room we fully enclosed the beam path. With such stability it is thus possible in the interaction room to use the wave front measured during the previous high-energy shot to correct the phase for the next shot.

We also measured the focal spot in the interaction chamber with a high-quality plane mirror instead of the deformable mirror. The focal spot comprised several hot spots [Fig. 1(a)], and the Strehl ratio was <0.1.

D. Beam Focus Optimization and Single-Hot-Spot Generation

Because we did not have a probe beam that propagates all along the chain, we had to make convergence loops with 70 J shots every 20 min. As mentioned above, because the laser thermal phase was stable we could use a previous shot as an error signal to feed the loop for the next shot. Fortunately, the loop converged in fewer than four iterations, as shown in Fig. 6, where we display the evolution of the far-field pattern during the convergence and plot the evolution of the associated Strehl ratio and of the wave-front PtV. Moreover, because the phase distortions of the laser chain are stable as long as the chain is fired at its nominal rate, one can sustain the correction for hours, once the convergence is achieved, by keeping the voltages that drive the DM fixed, as we observed throughout a 4-week experimental campaign.

For the final state of the convergence sequence [Fig. 6(h)], we plot in Fig. 7 the azimuthally averaged radial profile and the encircled energy within circles of increasing radius. The focal spot, averaged over several outputs of the convergence process, had a FWHM of 9.8 μm (with a rms of 0.7), with 35% of the energy within the central peak. The best Strehl ratio was 0.6, which means that the peak intensity could reach $\sim 2 \times 10^{16}$ W cm^{-2}. Moreover, we measured that the beam diameter changed by a factor of 2 over a distance of ~400 μm on either side of the best focus.

We now compare the Strehl ratio experimental value with the expected ratio. We estimated the latter by computing the point-spread function for the final state of convergence as given by the measured intensity and phase maps. These maps were extracted from the interferogram given by the ATWLSI. The result is shown in Fig. 3. Such a simulated focal spot should have a Strehl ratio of 0.7. Note that this expected best result of 0.7 for the system is less than the Strehl ratio that the DM was able to produce when it was used with the cw collimator, i.e., 0.85. This result could be due to shot-to-shot phase fluctuations (because the error signal is based on the phase of the previous shot), to the system's B integral ($B = 3$) that degrades the beam's near-field intensity profile [Fig. 3(a)], or to both. We can evaluate the relative importance of these two effects by simulating the focal spot as in Fig. 3 but using a flat near field, i.e., taking into account only the shot-to-shot phase fluctuations and not the B-integral effect. Such a simulated focal spot has a Strehl ratio of 0.7, demonstrating that shot-to-shot fluctuations are thus the main factor in reducing the Strehl ratio's optimum performance in the closed loop.

Several factors can also explain the difference between the observed (0.6) and the expected (0.7) values for the focal spot Strehl ratio. First, the focusing optics are not perfect: Tested independently by use of a cw collimator, it exhibits a slight astigmatism, with a Strehl ratio of 0.85 at its best adjustment. Second, the focusing and collecting doublets are sensitive to any tilt from the autocollimated position because of their large apertures. It is difficult to obtain a perfect match in aligning these optics onto the laser axis because the repetition rate of the laser is fairly low. Hence these optics could have been slightly tilted with respect to the input beam axis, thus explaining the difference between the focal spot that was observed through a collection of optics and the expected quality of the same focal spot as given by the input beam parameters.

We conclude that in our experiment, because of the closed loop that relies on the previous shot as the error

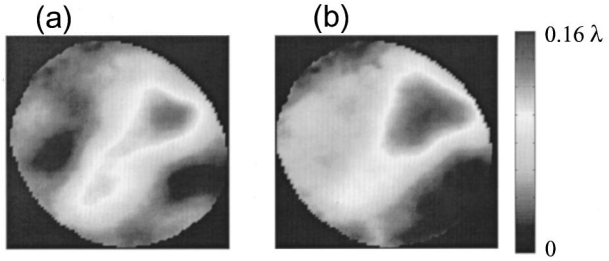

Fig. 5. Maps of the phase difference between the first shot in a regular sequence of 80-J shots every 20 min, and (a) the fourth shot in the same series and (b) the tenth shot in this series. The scale shows that the maximum shot-to-shot phase difference for a thermalized chain is ~0.15λ. Such stability of the laser wave front allows the wave front measured during the previous high-energy shot to be used to correct the phase for the next shot in the feedback loop system.

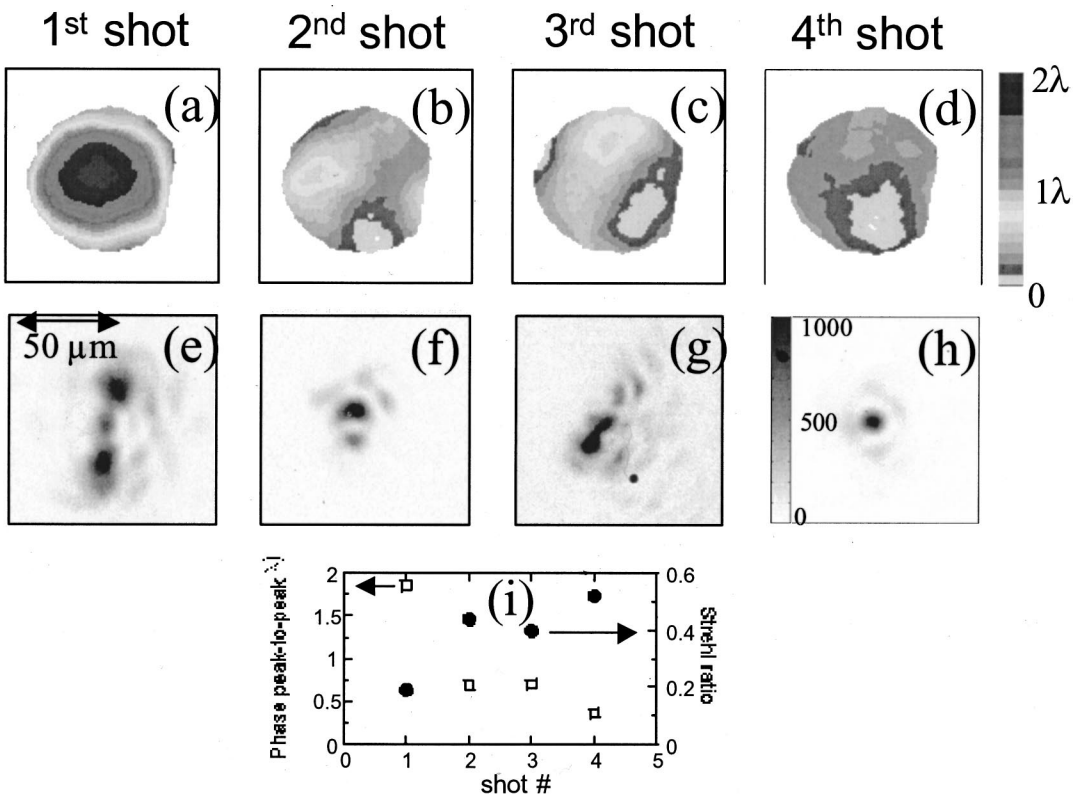

Fig. 6. (a)–(d) Wave-front phase maps of high-energy shots (50 J) during a converging sequence of the adaptive optics system. The color scale applies for all images (a)–(d). (e)–(h) Far-field patterns for the *same* shots (each focal spot is placed below the phase map to which it corresponds). The gray scale in (h) applies only to this image. (i) Corresponding evolution of the amplitude of the maximum wave-front distortion (squares, left scale) and of the Strehl ratio (filled circles, right scale).

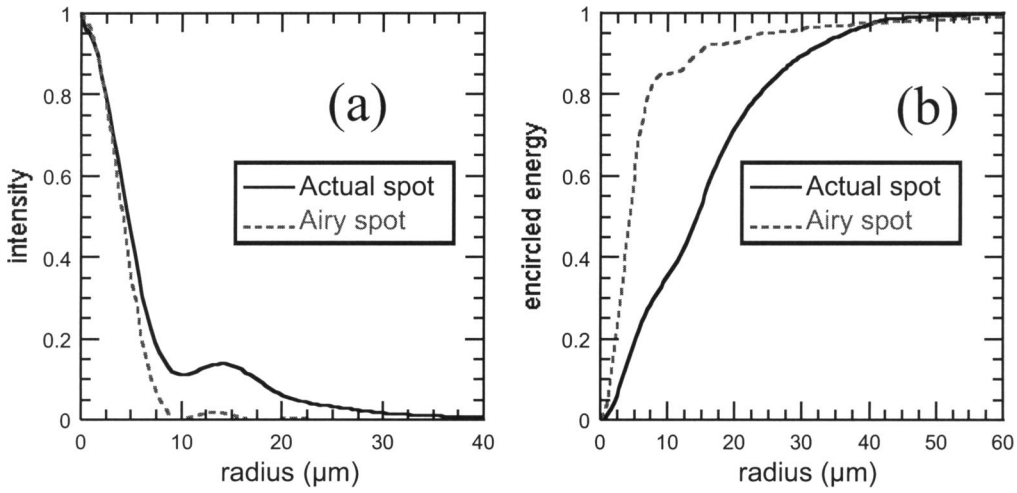

Fig. 7. (a) Solid curve, azimuthally averaged intensity profile of the focal spot at the end of the convergence [this profile is averaged over several shots, like the one shown in Fig. 6(h)]; dashed curve, same for the theoretical Airy spot. (b) Encircled energy as a function of radius for the profiles shown in (a); 35% of the incident energy is within the central peak of the actual focal spot, compared to 84% for the theoretical Airy spot.

signal in the loop, the best Strehl ratio that could be achieved is 0.7. Further degradation of the Strehl ratio to 0.6, as measured by the image of the far field, is due to the quality of both the focusing and the imaging optics.

The experimental Strehl ratio of 0.6, measured at full power and at the target location, needs to be compared to the <0.1 measured during shots without any correction. This means that the peak intensity was raised by a factor 6. Considering that usually this kind of laser is focused with a RPP in the beam, which means that the focal spot is more than ten times larger than the diffraction limit, we could then expect a laser–plasma interaction in an intensity regime almost 3 orders of magnitude greater than in the usual conditions.

3. COMPARATIVE STUDY OF SINGLE HOT SPOT AND RPP BEAM PROPAGATION IN AN UNDERDENSE PLASMA

A. Setup and Parameters of the Experiment

As mentioned above, the experiment uses four beams at the LULI laser facility. All beams are in the horizontal plane, with 600-ps FWHM Gaussian pulses. The plasma is generated by explosion of 1.2-μm thick, 380-μm-diameter free-standing CH (parylene *N*) disks. Two counterpropagating, 526-nm-wavelength laser beams that irradiate the target surface are used. RPP's that produce focal spots larger than the target are used on the beams. A third, identical beam, delayed by 0.6 ns with respect to the first two beams, further heats the plasma. The interaction beam (at $\lambda_0 = 1.053$ μm), to which wave front is corrected, is focused along the principal axis of plasma expansion and delayed by 1.6 ns with respect to the plasma-formation pulses. The focusing point is kept at the initial target plane. Either this beam can be used in the SHS configuration detailed above, with a maximum peak intensity of 2×10^{16} W cm^{-2}, or, alternatively, a 2-mm element RPP can be inserted in the beam's path before the $f = 500$ mm focusing doublet to produce a standard speckled distribution in the focal spot.[7] In this configuration the beam diameter is 320 μm (at FWHM), producing an average peak intensity of 10^{14} W cm^{-2} (i.e., it is the intensity of the most numerous speckles within the distribution).

The initial conditions of the preformed plasma have been extensively characterized and were reported previously.[36] The initial electron temperature (without interaction beam) is ~0.6 keV. The electron density at the top of the plasma profile decreases exponentially in time, $n_{top}/n_c \sim 0.13 \exp(-t[\text{ps}]/530)$, where $n_c = 10^{21}$ cm^{-3} is the critical electron density at $\lambda = 1053$ nm and $t = 0$ corresponds to the peak of the interaction pulse. The typical scale length of the plasma's parabolic profile is 700 μm.

The propagation of the interaction beam and its interaction with the underdense preformed plasma are diagnosed by use of several stations. The time-integrated far field of the beam in the output of the plasma is analyzed with the same station described above, which monitors the far field of the interaction beam in vacuum (with a collecting aperture that is twice the focusing aperture). Spatial integration of these images is used to measure the transmission rate of the interaction beam. To analyze the time-resolved spectra of the forward-scattered light we send a fraction of it to a spectrometer–streak camera combination, with spectral and temporal resolutions of 0.2 nm and 30 ps, respectively. Backscattered light, originating from either stimulated Brillouin scattering (SBS) or stimulated Raman scattering[3] (SRS), is also monitored in energy and spectrum.

B. Results

Figure 8 shows the comparative transmission rate, through the preformed plasma, of the SHS beam as a function of its incident peak intensity and of the RPP beam that had a mean peak intensity of $I_{avg} = 10^{14}$ W cm^{-2}. These transmission values were measured in a fixed collecting aperture that was twice the focusing aperture, centered on the beam axis. Note in particular that we did not measure light that could be transmitted but was scattered at larger angles. The intensity distribution[7] of the RPP beam is graphically presented in Fig. 8, overlaid on the transmission data point, showing the extension of the incident peak intensities of the speckles within the vacuum focal pattern. The highest peak intensity within this distribution is $\sim 11 \times I_{avg} = 1.1 \times 10^{15}$ W cm^{-2}: For higher-intensity values the expected number of speckles is smaller than 1. These preliminary (because of the limited amount of data points) results seem to show that the RPP beam transmission level is above the level of the SHS beams that have intensities within the range of the RPP beam's intensity distribution. This result would imply that the behavior of a RPP beam composed of numerous speckles does not result from the linear superposition of all these speckles.

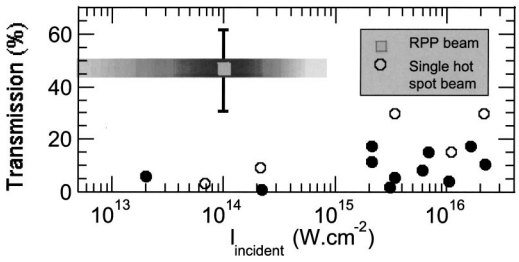

Fig. 8. Transmission rate within the *f*/3 collecting cone and through the plasma ($\sim 0.1\, n_c / \sim 1$ mm) of the SHS beam (filled and open circles, which represent two series of shots) as a function of the incident peak intensity and of the RPP beam at its nominal mean intensity (10^{14} W cm^{-2}). Overlaid upon the RPP data point (averaged over four shots) is the vacuum intensity distribution of the speckles within the focal pattern (linear gray scale). The error bar on the RPP data point represents the shot-to-shot variation. The collecting optics' aperture is twice the focusing aperture.

Several hypotheses could explain the difference in the overall propagation between the RPP beam and the SHS beam. First, there could be cross-talk effects between overlapping individual filaments. Cross talk can be generated by induced density perturbations from each speckle, which have wings that can spread to many times a filament's radius.[37] Thus it can add a random phase shift to the electromagnetic field in neighbor filaments as well as perturb the overall hydrodynamics.[38] Another possibility stems from either the mode instability of the individual filaments or the filamentation of the individual speckles, which redirects the light, resulting in a blend of light coming from different filaments. The heating of the plasma is also not the same in the two cases: the SHS beam heats the plasma locally, whereas the RPP beam induces a heating over a large zone. The consequence of these effects, observed in numerical simulations[39–41] but not taken into account in analytical models[42] of LPI growth, lies in the modification of the overall laser–plasma coupling for the RPP beam compared with the linear superposition of the individual filaments' response. Another effect that could modify the propagation of the RPP beam compared to that of the SHS is the existence of a different scale length, i.e., the large overall envelope of

the beam (typically a few hundred micrometers), inducing, for example, self-focusing of the whole beam.[14,43] Also, we have to remember that the SHS beam is continuous along the propagation axis, whereas the speckles of the RPP beam have a finite extension on the same axis that is, on average, ~470 μm.

We now look in more detail at the physical mechanisms at play in SHS beam propagation. For this beam, neither backscattered processes nor absorption by means of inverse bremsstrahlung heating seem to be able to account for the observed transmission levels. Indeed, backscattered energy levels are below 1% for both stimulated Brillouin scattering and stimulated Raman scattering for all the intensities explored, and inverse bremsstrahlung calculations give a maximum absorption of ~0.45. This number is maximized by use of an electron temperature of 0.6 keV because the heating induced by the interaction beam itself[19] can significantly increase this temperature, which in turn leads to lower absorption. Low transmission of the SHS beam could alternatively result from filamentation and forward stimulated Brillouin scattering[2,44–46] (FSBS) that induce beam breakup and energy spreading at large angles.

Beam breakup of the SHS beam is indeed observed in the experiment, as illustrated in Fig. 9(a), where we plot the evolution of the encircled energy within a disk of 25-μm radius centered about the peak intensity, as measured from the spatial distribution of the energy in the far field. We can observe that beam breakup grows; i.e., increasingly more energy is spread over a large area as the incident intensity increases. Such breakup of the SHS beam with incident intensities of 10^{13}–10^{15} W cm^{-2} demonstrates that overlap between the filaments in the RPP beam is most probable because in this range of intensity the far field of the SHS is seen to extend by more than the mean separation between the speckles in the RPP beam.

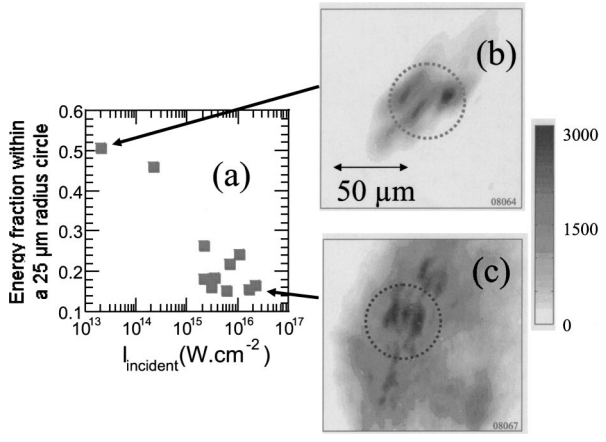

Fig. 9. (a) Fraction, within a circle of 25-μm radius, of the transmitted energy of the SHS beam through the plasma as a function of the incident peak intensity. The fraction of the incident energy contained within the same area is ~0.8 [Fig. 7(b)]. (b) Time-integrated far-field pattern of the light in the output of the plasma. The incident intensity is 2×10^{13} W cm^{-2}. Superimposed is the 25-μm-radius circle in which the energy fraction plotted in (a) is measured. (c) Same as (b) but for an incident intensity of 2×10^{16} W cm^{-2}. Each image corresponds to a data point in (a) to which an arrow points. The gray scale applies for (b) and (c).

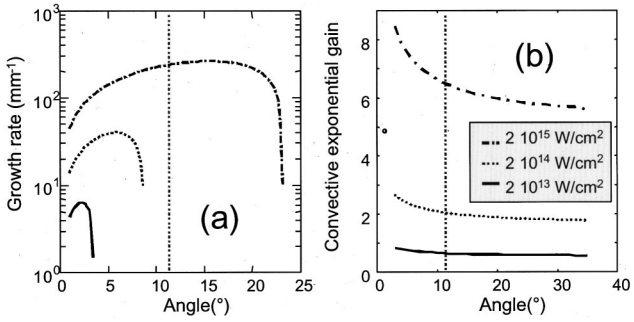

Fig. 10. Steady-state calculated values as a function of the angle (from forward) of the scattered electromagnetic wave of (a) the filamentation spatial growth rate[37,47,48,52] and (b) forward SBS convective exponential gain.[37,53,54] These values were calculated, with the experimental parameters, for three incident intensities and include nonlocal transport effects. The vertical dotted line represents the collecting optics' aperture.

Extensive theoretical and experimental studies have been made of laser filamentation, FSBS, and self-focusing in plasmas. Numerical simulations[2,45] have shown that, as these phenomena develop, they can lead to complicated, time-dependent laser intensity and plasma density distributions inside the plasma. However, the relative importance of these instabilities can be evaluated before this complex stage is reached, i.e., for sufficiently low intensities, by use of steady-state analytical estimates.

Filamentation and FSBS are closely related and have growth rates of comparable magnitude (a fraction of an inverse picosecond in our conditions). Filamentation involves the decay of the pump wave into two scattered electromagnetic waves, propagating symmetrically at angles of $\pm\theta$, and a quasi-static density perturbation. When filamentation is growing, it amplifies the level of the initial modulations and breaks the beam into small filaments. FSBS is a three-wave resonant instability in which the scattered electromagnetic wave coupled to the pump wave drives traveling acoustic waves. Density modulations induced by the ponderomotive and thermal pressures of the initially inhomogeneous beam provide a seed for both instabilities. These modulations can also act to self-focus the beam and raise its intensity, which, in turn, will exacerbate the growth of filamentation and FSBS.

Self-focusing of the SHS beam is likely to occur even at the lowest intensity because thermal effects, in particular nonlocal[20,47,48] ones, are important in our experimental conditions.[36,42,49] Heat conduction is nonlocal, as the mean free path of the electrons is larger than the typical scale length of the temperature perturbation. Under these conditions heat conduction is reduced and the local thermal pressure increased. Thus much lower power than in the collisionless (ponderomotive only) situation[37] is required for creation of a self-focused filament. More precisely, calculations[42] show that in our conditions the threshold to an increase of twice the beam intensity is only $\sim 0.1 I_{\mathrm{pond}} \sim 3 \times 10^{13}$ W cm^{-2}, where I_{pond} corresponds to the ponderomotive threshold.

The behavior of filamentation and FSBS as functions of the incident intensity and of the angle of the scattered light wave as well as their low thresholds are illustrated in Fig. 10. The figure shows that, compared to FSBS,

filamentation is restricted to smaller deflection angles because the growth rate is maximized for a well-defined scattering angle. However, the scattering angle also increases with the incident intensity, as shown in Fig. 10(a). Starting from the finite-angle incident pump, filamentation widens the angular distribution of the transmitted light and can serve as a feedback to FSBS. As the incident intensity increases, FSBS and filamentation are more strongly excited at increasingly larger angles (Fig. 10), leading to more energy spread outside the collecting optics.[44,45]

Other processes such as hosing instability[16,17] and filament mode instability[18] can also play significant roles in the propagation of the SHS beam. Mode instability, whose onset competes with filamentation's early stage, involves coupling, within the deep density channel bored by the beam, between the fundamental propagating mode and the excited eigenmodes of the waveguide. It is characterized by a strong growth rate, larger than that for FSBS. As a result of the instability, the light is untrapped from the channel into a resonantly excited mode. The channel is then disrupted.

These processes could prove to be important, particularly at high intensity, as suggested by the time-resolved spectra of the light scattered forward. Figure 11 shows spectra for the SHS beam at several incident intensities. It displays two components: The unshifted component results either from scattering of untrapped light on stationary density fluctuations produced by filamentation or by self-focusing or from FSBS because the shift that it would produce at the observed angle (=0.12 nm) is within the diagnostic's spectral resolution. The redshifted component can be explained[42,50] by a combination of FSBS growing in a modified regime at high intensity,[39,45] hosing instability, and self-phase modulation.[18,51] Self-phase modulation involves rapidly decreasing density within the self-dug channel along which the beam propagates, which gives rise to a modified phase and thus to a red spectral shift. Hosing instability can further enhance this redshift because of an increased path length within the curving channel. Two differences, however, can be seen between the high-intensity (2×10^{16} W cm^{-2}) spectrum [Fig. 11(a)] and the lower-intensity (2×10^{14} W cm^{-2}) spectrum [Fig. 10(c)]. The first is not only shifted further to the red but also exhibits some bursts that move in time from shot to shot along its temporal evolution. In comparison, the spectrum of the transmitted RPP (multispeckled) beam at $I_{avg} = 10^{14}$ W cm^{-2} displayed in Fig. 11(e) does not exhibit similar temporal bursts. The stronger redshift shown in Fig. 11(a) could result from the deepening and lengthening of the density channel with rising intensity. The burstlike nature could be understood as the result of the filament's mode instability[18]: As the light is abruptly untrapped from the channel when the instability is triggered, its phase is no longer modified by the time-dependent deepening of the channel, resulting in a disruption of the spectral redshift. The fact that this instability requires a channel deep enough to support other modes could explain why we observe this behavior only at high intensity. Experiments at still higher intensities could be useful for further study of the behavior of this instability.

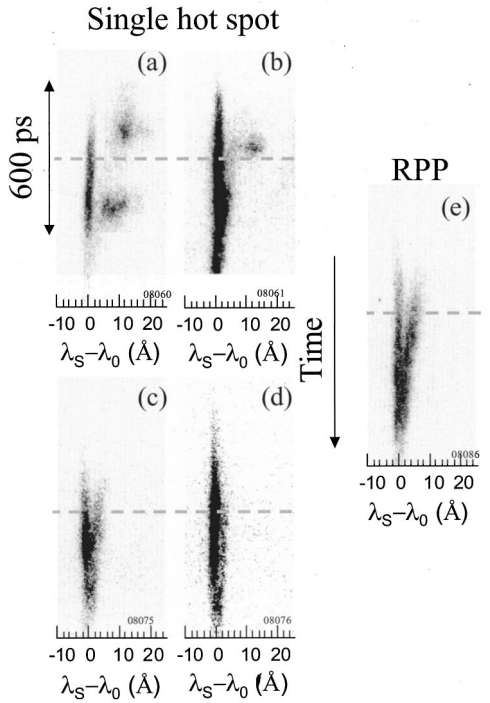

Fig. 11. Spectra of the light scattered forward, after propagation through the plasma, in a ring from 7° to 11° about the incident axis (i.e., outside the incident cone). (a) SHS beam with an incident intensity of 2×10^{16} W cm^{-2} ($T = 18\%$). (b) SHS beam with an incident intensity of 2×10^{15} W cm^{-2} ($T = 18\%$). (c) SHS beam with an incident intensity of 2×10^{14} W cm^{-2} ($T = 9\%$). (d) SHS spot beam with an incident intensity of 6×10^{13} W cm^{-2} ($T = 3\%$). (e) RPP beam with a mean incident intensity of 10^{14} W cm^{-2}. Horizontal dashed lines indicate the temporal peak of the incident pulse.

4. CONCLUSIONS

We have experimentally demonstrated efficient wave-front correction of one beam of the Laboratoire pour l'Utilisation des Lasers Intenses six-beam high-energy (100-J, 1-ns) Nd:glass laser facility with an adaptive optical system. Compared to the focal pattern composed of several spots produced by the uncorrected beam with a Strehl ratio of <0.1, the peak intensity of corrected shots is enhanced by a factor of 6, with a Strehl ratio of ~ 0.6. Our system uses a large-aperture dielectric-coated deformable mirror that allows the thermal distortions of the laser chain to be corrected just before the target chamber and thus avoids the inherent limitations associated with precompensation of aberrations when the corrector is placed upstream in the chain of amplifiers. We tested two wave-front sensors (a Shack-Hartmann sensor and a three-wave lateral shearing interferometer) in our system. We found that the use of the interferometer significantly improves the stability of the whole system: As the measured integrated phase can be downsampled to match the resolution of the deformable mirror, the issues related to the precise alignment of the wave-front sensor are virtually eliminated. Our correction capability is currently limited by the absence of an auxiliary beam that could probe the phase status of the laser before a shot and, ul-

timately, by the B integral of the system. We found that the final quality of the focal spot is also limited by the quality of the focusing and imaging optics, which further degrades the observed Strehl ratio compared with the expected ratio that we measured by simulating the focal spot, using the phase and intensity distributions before the focusing optics.

We have used this system to study beam propagation in a plasma, a topic of significant interest in the context of internal confinement fusion. The SHS beam breaks up during propagation as a result of various instabilities that are essentially time dependent and act as to spread the beam angularly and spectrally. Also at play is the filament's instability, which can abruptly disrupt the propagated mode. When the SHS beam and a conventional RPP beam composed of many speckles that have various intensities are compared, the interaction between those speckles within the focal distribution seems to play an important role in propagation of the RPP beam such that it does not behave as a superposition of individually propagating filaments.

More generally, a direct comparison of experiment and modeling in the case of a single hot spot should help to enable this system better to isolate fundamental processes implied in LPI for the large smoothed (RPP-like) beams. This could in turn enhance the quantitative predictability of LPI for future megajoule ICF facilities.

ACKNOWLEDGMENTS

We acknowledge useful discussions with V. Tikhonchuk, D. Pesme, S. Hüller, and A. Maximov. We also gratefully acknowledge the support of the LULI technical teams, in particular, A. Michard for help in implementing the system and P. Moreau and L. Martin for laser operation. This study was partly supported by European Adaptool Research and Technological Development contract HPRI-CT-1999-50012.

*Present address, Phasics S.A., Campus de l'Ecole Polytechnique, 91128 Palaiseau cedex, France.

†Present address, General Atomics, P.O. Box 85608, San Diego, California 92186-5608; e-mail: fuchsj@fusion.gat.com.

‡Present address, Departement de Physique Theorique et Appliquee, Commissariat à l'Energie Atomique–Direction Ile-de-France, 91680 Bruyeres-le-Chatel cedex, France.

REFERENCES

1. W. Koechner, "Thermal effect in laser rods," in *Solid-State Laser Engineering*, D. L. MacAdam, ed. (Springer-Verlag, Berlin, 1976), pp. 365–382.
2. P. E. Young, "Laser beam propagation and channel formation in underdense plasmas," Phys. Plasmas **2**, 2825–2834 (1995).
3. W. L. Kruer, *Physics of Laser Plasma Interactions* (Addison-Wesley, Reading, Mass., 1988).
4. J. Lindl, "Development of the indirect-drive approach to inertial confinement fusion and the target physics basis for ignition and gain," Phys. Plasmas **2**, 3933–4024 (1995).
5. J. D. Lindl, *Inertial Confinement Fusion. The Quest for Ignition and Energy Gain Using Indirect Drive* (Springer-Verlag, New York, 1998).
6. Y. Kato, K. Mima, N. Miyanaga, S. Arinaga, Y. Kitagawa, M. Nakatsuka, and C. Yamanaka, "Random phasing of high-power lasers for uniform target acceleration and plasma instability suppression," Phys. Rev. Lett. **53**, 1057–1059 (1984).
7. J. Garnier, "Statistics of the hot spots of smoothed beams produced by random phase plates revisited," Phys. Plasmas **6**, 1601–1610 (1999).
8. Laboratory for Laser Energetics, University of Rochester, "Phase conversion using distributed polarization rotation," Vol. 45 of LLE Review (National Technical Information Services, Springfield, Va., 1990).
9. K. Tsubakimoto, M. Nakatsuka, H. Nakano, T. Kanabe, T. Jitsuno, and S. Nakai, "Suppression of interference speckles produced by a random phase plate using a polarization control plate," Opt. Commun. **91**, 9–12 (1992).
10. R. Lehmberg and S. Obenschain, "Use of induced spatial incoherence for uniform illumination of laser fusion targets," Opt. Commun. **46**, 27–31 (1983).
11. R. Lehmberg, A. Schmitt, and S. Bodner, "Theory of induced spatial incoherence," J. Appl. Phys. **62**, 2680–2701 (1987).
12. S. Skupsky, R. Short, T. Kessler, R. Craxton, S. Letzring, and J. Soures, "Improved laser beam uniformity using the angular dispersion of frequency modulated light," J. Appl. Phys. **66**, 3456–3462 (1989).
13. D. Veron, G. Thiell, and C. Gouédard, "Optical smoothing of the high power PHEBUS Nd-glass laser using the multimode optical fiber technique," Opt. Commun. **97**, 259–271 (1993).
14. C. Still, R. Berger, A. Langdon, D. Hinkel, L. Suter, and E. Williams, "Filamentation and forward Brillouin scatter of entire smoothed and aberrated laser beams," Phys. Plasmas **7**, 2023–2032 (2000).
15. E. Valeo, "Stability of filamentary structures (e.m. wave propagation in plasma)," Phys. Fluids **17**, 1391–1393 (1974).
16. E. Valeo and K. Estabrook, "Stability of the critical surface in irradiated plasma," Phys. Rev. Lett. **34**, 1008–1010 (1975).
17. C. Ren and W. B. Mori, "Physical picture for the laser hosing instability in a plasma," Phys. Plasmas **8**, 3118–3119 (2001).
18. D. Pesme, W. Rozmus, V. Tikhonchuk, A. Maximov, I. Ourdev, and C. Still, "Resonant instability of laser filaments in a plasma," Phys. Rev. Lett. **84**, 278–280 (2000).
19. O. V. Batishchev, V. Y. Bychenkov, F. Detering, W. Rozmus, R. Sydora, C. E. Capjack, and V. N. Novikov, "Heat transport and electron distribution function in laser produced plasmas with hot spots," Phys. Plasmas **9**, 2302–2310 (2002), and references therein.
20. A. Brantov, V. Bychenkov, V. Tikhonchuck, and W. Rozmus, "Nonlocal electron transport in laser heated plasmas," Phys. Plasmas **5**, 2742–2753 (1998).
21. S. Cameron and J. Camacho, "Characterization of heat transport dynamics in laser-produced plasmas using collective Thomson scattering: simulation and proposed experiment," J. Fusion Energy **14**, 373–388 (1995).
22. D. Montgomery, R. Johnson, J. Cobble, J. Fernandez, E. Lindman, H. Rose, and K. Estabrook, "Characterization of plasma and laser conditions for single hot spot experiments," Laser Part. Beams **17**, 349–359 (1999).
23. D. S. Montgomery, R. P. Johnson, H. A. Rose, J. A. Cobble, and J. C. Fernández, "Flow-induced beam steering in a single laser hot spot," Phys. Rev. Lett. **84**, 678–680 (2000).
24. F. Roddier, *Adaptive Optics in Astronomy* (Cambridge U. Press, Cambridge, 1999).
25. F. Druon, G. Chériaux, J. Faure, J. Nees, M. Nantel, A. Maksimchuk, G. Mourou, J.-C. Chanteloup, and G. Vdovin, "Wave-front correction of femtosecond terawatt lasers by deformable mirrors," Opt. Lett. **23**, 1043–1045 (1998).
26. D. M. Pennington, C. G. Brown, T. E. Cowan, S. P. Hatchett, E. Henry, S. Herman, M. Kartz, M. Key, J. Koch, A. J. MacKinnon, M. D. Perry, T. W. Phillips, M. Roth, T. C. Sangster, M. Singh, R. A. Snavely, M. Stoyer, B. C. Stuart,

and S. C. Wilks, "Petawatt laser system and experiments," IEEE J. Sel. Top. Quantum Electron. **6**, 676–688 (2000).
27. J.-C. Chanteloup, H. Baldis, A. Migus, G. Mourou, B. Loiseaux, and J.-P. Huignard, "Nearly diffraction-limited laser focal spot obtained by use of an optically addressed light valve in an adaptive-optics loop," Opt. Lett. **23**, 475–477 (1998).
28. J.-C. Chanteloup, F. Druon, M. Nantel, A. Maksimchuk, and G. Mourou, "Single-shot wave-front measurements of high-intensity ultrashort laser pulses with a three-wave interferometer," Opt. Lett. **23**, 621–623 (1998).
29. J. Primot and L. Sogno, "Achromatic three-wave (or more) lateral shearing interferometer," J. Opt. Soc. Am. A **12**, 2679–2685 (1995).
30. A. V. Kudryashov and V. I. Shmalhausen, "Semipassive bimorph flexible mirrors for atmospheric adaptive optics applications," Opt. Eng. **35**, 3064–3073 (1996).
31. J. Fuchs, B. Wattellier, J. P. Zou, J. C. Chanteloup, H. Bandulet, P. Michel, and C. Labaune, "Wave front correction for near diffraction-limited focal spot on a 6 × 100 J/1 ns laser facility," in *Laser Applications and Technologies*, A. A. Mak and V. Ya. Panchenko, eds., Proc. SPIE (to be published).
32. K. Strehl, "Uber Luftschlieren und Zonenfehler," Zeitschrift Instrumentenkunde **22**, 213–223 (1902). It is the ratio of the peak intensity at the focus of the beam with the given (distorted) wave front and its near-field intensity profile, to that of the same near-field intensity distribution with a flat wave front.
33. B. Wattellier, "Amélioration des performances des chaînes lasers solides utilisant l'amplification à dérive de fréquence: nouveaux réseaux de diffraction à haute tenue au flux et mise en forme programmable de faisceaux lasers par modulation de la phase spatiale," Ph.D. dissertation (Ecole Polytechnique, Palaiseau, France, 2001).
34. W. Koechner, "Damage of optical elements," in *Solid-State Laser Engineering*, D. L. MacAdam, ed. (Springer-Verlag, Berlin, 1976), pp. 546–549.
35. B. Wattellier, J.-C. Chanteloup, J. Fuchs, C. Sauteret, J. P. Zou, and A. Migus, "Wave front correction and focusing optimization of partially thermalized Nd:glass high power CPA laser," in *Conference on Lasers and Electro-Optics*, OSA 2001 Technical Digest Series (Optical Society of America, Washington, D.C., 2001), pp. 70–71.
36. J. Fuchs, C. Labaune, S. Depierreux, V. Tikhonchuk, and H. Baldis, "Stimulated Brillouin and Raman scattering from a randomized laser beam in large inhomogeneous collisional plasmas. I. Experiment," Phys. Plasmas **7**, 4659–4668 (2000).
37. V. Bychenkov, W. Rozmus, A. Brantov, and V. Tikhonchuk, "Theory of filamentation and stimulated Brillouin scattering with nonlocal hydrodynamics," Phys. Plasmas **7**, 1511–1519 (2000).
38. B. Bezzerides, H. X. Vu, and R. A. Kopp, "Hydrodynamic coupling of a speckled laser beam to an axially flowing plasma," Phys. Plasmas **8**, 249–259 (2001).
39. A. Schmitt and B. Afeyan, "Time-dependent filamentation and stimulated Brillouin forward scattering in inertial confinement fusion plasmas," Phys. Plasmas **5**, 503–517 (1998).
40. A. Schmitt, "The effects of optical smoothing techniques on filamentation in laser plasmas," Phys. Fluids **31**, 3079–3101 (1988).
41. S. Hüller, P. Mounaix, V. Tikhonchuk, and D. Pesme, "Interaction of two neighboring laser beams taking into account the effects of plasma hydrodynamics," Phys. Plasmas **4**, 2670–2680 (1997).
42. V. Tikhonchuk, J. Fuchs, C. Labaune, S. Depierreux, S. Hüller, J. Myatt, and H. Baldis, "Stimulated Brillouin and Raman scattering from a randomized laser beam in large inhomogeneous collisional plasmas. II. Model description and comparison with experiments," Phys. Plasmas **8**, 1636–1649 (2001).
43. T. Afshar-rad, L. Gizzi, M. Desselberger, F. Khattak, O. Willi, and A. Giulietti, "Evidence for whole-beam self-focusing of induced spatially incoherent laser light in large underdense plasma," Phys. Rev. Lett. **68**, 942–944 (1992).
44. S. Wilks, P. Young, J. Hammer, M. Tabak, and W. Kruer, "Spreading of intense laser beams due to filamentation," Phys. Rev. Lett. **73**, 2994–2997 (1994).
45. V. V. Elisseev, I. Ourdev, W. Rozmus, V. Tikhonchuk, C. Capjack, and P. Young, "Ion wave response to intense laser beams in underdense plasmas," Phys. Plasmas **4**, 4333–4346 (1997).
46. P. E. Young, M. Foord, J. Hammer, W. Kruer, M. Tabak, and S. Wilks, "Time-dependent channel formation in a laser-produced plasma," Phys. Rev. Lett. **75**, 1082–1085 (1995).
47. E. M. Epperlein, "Kinetic theory of laser filamentation in plasmas," Phys. Rev. Lett. **65**, 2145–2148 (1990).
48. E. M. Epperlein and R. W. Short, "Nonlocal heat transport effects on the filamentation of light in plasmas," Phys. Fluids B **4**, 2211–2216 (1992).
49. J. Myatt, D. Pesme, S. Hüller, A. Maximov, W. Rozmus, and C. Capjack, "Nonlinear propagation of a randomized beam through an expanding plasma," Phys. Rev. Lett. **87**, 255003 (2001).
50. J. Fuchs, C. Labaune, S. Depierreux, H. Baldis, A. Michard, and G. James, "Experimental evidence of plasma-induced incoherence of an intense laser beam propagating in an underdense plasma," Phys. Rev. Lett. **86**, 432–434 (2001).
51. C. Yamanaka, T. Yamanaka, J. Mizui, and N. Yamaguchi, "Self-phase modulation of laser light in a laser-produced plasma," Phys. Rev. A **11**, 2138–2141 (1975).
52. P. E. Young, "Experimental observation of filamentation growth in laser-produced plasmas," Phys. Plasmas **2**, 2815–2824 (1995).
53. R. W. Short and E. M. Epperlein, "Thermal stimulated Brillouin scattering in laser-produced plasmas," Phys. Rev. Lett. **68**, 3307–3310 (1992).
54. E. Williams, "Convective growth of parametrically unstable modes in inhomogeneous media," Phys. Fluids B **3**, 1504–1506 (1991).